JOURNAL OF MATERIALS SCIENCE 30 (1995) 3098–3110

Analysis of the tensile properties and fractography of as-cast and heat treated 359–SiC–20p composite

A. M. SAMUEL, F. H. SAMUEL
Département des Sciences Appliquées, Université du Québec à Chicoutimi, Chicoutimi, Québec, Canada, G7H 2B1

An experimental study of the heat treatment of 359–SiC–20p composite and its base alloy was made to determine the strength–ductility characteristics under varying conditions of heat treatment. Microstructural observations revealed that addition of the SiC_p reinforcement to the base alloy produced a more uniform and refined interdendritic microstructure compared to the latter. The tensile data obtained was analysed in terms of the theoretical models existing in the composite literature. Ultimate tensile strength (UTS)–log elongation relationships were obtained to test the applicability of the quality index parameter, *Q*, to the present composite. From this analysis, it was found that all data points in the ageing temperature range 140–210 °C could be represented by a single line (cf. two lines in the case of 359 alloy), indicating the important fact that the tensile properties of this composite can be predicted/determined over the entire temperature range. The presence of the SiC particles was seen to accelerate the Mg_2Si precipitation kinetics, but not to alter it. Fracture mechanisms were determined from both the fracture surfaces and their longitudinal sections beneath the fracture surface, employing both optical and scanning electron microscopy.

Nomenclature

a	Particle diameter
b	Burger's vector
b_{ii}	Numerical constant relating $\langle P_{ii}^{E} \rangle_m$ and P_{33}^{A}
E_c	Young's modulus of the composite
E_m	Young's modulus of the matrix
E_p	Young's modulus of SiC particles
El	Elongation (%)
f_p	SiC volume fraction
P_{33}^{A}	Applied stress
$\langle P_{ii}^{E} \rangle$	Long range back stress developed by elastic misfit
ΔP_m^F	Change in matrix flow stress
$< P_{ii}^{P} >_m$	Back stresses due to plastic deformation
P_c^{ps}	Proof strain of a composite
q_{ii}	Plastic misfit
Q	Quality index
R	Statistical correlation coefficient
RE	Rockwell E hardness value
S	SiC particle aspect ratio
S_c	Critical aspect ratio for the SiC particles
UTS	Ultimate tensile strength of the alloy or composite
YS	Yield strength of the alloy or composite
α	Critical misfit strain
γ	Constant, 1.25 for aluminum alloys
ε	Plastic strain
ε^{ps}	Plastic strain at which P_c^{ps} is required
$\dot{\theta}$	Work hardening rate at a given plastic strain
$\ddot{\theta}$	Work hardening rate as a function of total strain
μ	Shear modulus
$\bar{\rho}$	Dislocation density
σ_c^0	Yield stress of the composite
$\Delta\sigma_{CTE}$	Increase in yield stress due to coefficient of thermal expansion (CTE)
σ_m^0	Yield stress of the matrix
σ_p	Particle strength
τ_i	Interfacial shear strength

1. Introduction

The mechanical properties of a metal matrix composite (MMC) are determined not only by the composition and properties of both matrix and reinforcement, but also by the chemical interactions at the reinforcement–matrix interface, the latter gaining particular significance in the case of composites cast from the melt [1, 2]. According to Chadwick, the mechanical testing of MMCs is not an uncomplicated process, and few systematic studies appear to have been conducted to separate matrix and interfacial effects when making general property evaluations [1]. In addition, unlike

0022–2461

continuous fibre reinforced MMCs, particulate reinforced MMCs do not follow a simple rule of mixtures (ROM) type of behaviour, and, in general, increased ductilities are usually obtained at the cost of a decrease in the strength level. The need for systematic, comprehensive data is thus obvious, if one is to select certain properties (or a property) to satisfy the end application requirements of a particular composite type.

During the last few years, several studies of the mechanical behaviour of discontinuously reinforced aluminum (DRA) alloy composites have been reported, where the effects of heat treatment, matrix microstructure and particulate reinforcement content on the mechanical properties have been investigated [3–6]. Most of these studies, however, have focused on fracture behaviour and have been conducted on SiCp reinforced Al composites possessing *wrought* Al alloy type matrices.

In the present study, a detailed investigation of the heat treatment of *cast* 359–SiC–20p composite was made in order to determine the optimum combination of strength–ductility that could be obtained from the corresponding mechanical properties–heat treatment condition. The work reported here forms part of an extensive programme on SiC particulate reinforced Al–Si–Mg composites being carried out at the Université du Québec à Chicoutimi. An analysis of the tensile properties and fracture behaviour is presented and discussed in terms of the data available on the heat treatment of both Al–Si–Mg (matrix) alloys and that of their MMCs.

2. Experimental procedure

The chemical compositions of the composite and that of its base alloy are shown in Table I. The composite material was received in the form of 12.5 kg ingots from Duralcan Canada. The ingots were cut into two halves and heated at 400 °C for 2 h prior to remelting. The cut pieces were charged to a 36 kg capacity silicon carbide crucible when the temperature inside the crucible reached 550 °C. To prevent SiC particle sedimentation during remelting, the melt was mechanically stirred using a graphite impeller designed especially for this purpose.

In the case of the base alloy 359, pure silicon and Al-50 wt % Mg master alloy were added to a 356 alloy melt, to bring the silicon and magnesium levels to those shown in Table I. The melt was degassed using a hollow graphite rotary impeller, running at 180 r.p.m, through which dry argon was passed into the melt.

For both composite and base alloy melts, the melt hydrogen level was monitored *in situ* using an Al-SCAN™ unit. In addition, for each pouring/casting, specimens were also cast simultaneously in Ransley moulds from which "Ransley" samples were machined for determination of hydrogen content using the Leco vacuum fusion technique. This is one of the standard methods for obtaining accurate analysis of the hydrogen content in a melt [7]. The analysis was carried out at Alcan International's Arvida R&D Centre, Jonquière, Québec.

In the two cases, the melts were filtered using ceramic foam filters (of 6 ppcm size for the composite and 8 ppcm size for the base alloy). Filters (3.3 cm diameter discs) were placed at the bottom of stainless steel tubes (15 cm in length) that comprised the external risers and which were heated at 600 °C prior to casting. The melt temperature was kept close to 735 °C, whereas the mould temperature (Stahl Mold, ASTM-B-108-85a [8]) was about 400–410 °C.

For each pouring, specimens for chemical analysis were taken from the central portion of the melt crucible. The as-cast test bars obtained from the Stahl mould castings (50 mm gauge length and 12.5 mm diameter) were subjected to various heat treatments comprising solution treatment (8 h at 540 °C or 24 h at 550 °C), quenching (water at 25 or 60 °C), natural ageing (0, 24 or 48 h) and artificial ageing (5 h at 155 °C).

The tempered test bars were subjected to tensile testing (under uniaxial tensile loading) at room temperature, employing an Instron testing machine and using a strain rate of $4 \times 10^{-4}\,s^{-1}$. A strain gauge extensometer (5.1 cm) was attached to the test specimens to measure elongation as the load was applied. For each tempered condition, at least ten test bar specimens were tested. Longitudinal samples were sectioned from the fractured test bars for microstructural examination of defects. All samples were polished using a technique specially developed for such composites.

Metallographic samples (transverse sections) were also obtained from the gauge length (central) portions of the tensile tested test bars from positions away from the fracture surface to examine the microstructural characteristics, using optical (Olympus PMG3) and scanning electron (Hitachi S-2700) microscopy. The eutectic silicon particle characteristics and volume fraction measurements of porosity and oxides present in these samples were measured using image analysis (Leco 2001 image analyser system attached to the optical microscope). These measurements were

TABLE I Chemical compositions (wt %) of the base alloy and composite

Alloy type	Element (wt %)							SiC_p (vol %)
	Si	Mg	Fe	Cu	Mn	Ti	Sr	
Base (359)	10.2	0.70	0.10	0.018	0.004	0.09	0.015	–
Composite (359–SiC–20p)	9.4	0.59	0.14	0.010	0.004	0.10	0.009	20.9

performed in the usual manner as that employed for volume fraction or other feature measurements of any specified phase (see [9] for details).

3. Results and discussion

3.1. Microstructure

The as-cast microstructures of the base alloy and composite are shown in Fig. 1a, b, respectively. The Sr content in the base alloy (359) was maintained constant at 150 p.p.m., with the addition of Al–10 wt% Sr master alloy to the melt from time to time; whereas in the composite alloy, the Sr level was determined to be 90 p.p.m. from chemical analysis.

The eutectic silicon particle characteristics obtained for as-cast and solution heat treated samples (8 h at 540 °C followed by quenching in warm water at 60 °C) of the matrix alloy and composite are shown in Fig. 2. As one may note from Figs 1 and 2, and as was generally observed, the number of silicon particles is much less in the composite sample than in the base alloy. This can be understood by referring to the as-cast microstructures. The base alloy specimen, Fig. 1a, clearly shows the presence of large interdendritic regions, where there is a concentration of the silicon particles. These regions are randomly dispersed over the specimen surface. The composite sample, however, displays a much more uniform distribution of the interdendritic regions, Fig. 1b, and the regions themselves are seen to be much smaller. In addition, in the composite, these interdendritic regions have to accommodate both Si particles and the SiC reinforcement. Thus, effectively, on a one-to-one basis, there will be lesser Si particles observed in the composite sample than in the base alloy for the same area scanned. However, because the silicon level remains the same in both alloys, the silicon particle distribution will have to be rearranged to accommodate the same silicon level in the composite. This appears to be accomplished by the uniform–smaller interdendritic region pattern exhibited by the solidification structure of the composite. Bayoumi and Suéry also reported observations of the acceleration of the transformation of dendritic structure into a globular one in Al–7Si–0.3 Mg–SiC_p composites compared to the matrix alloy [10]. According to Mortensen and Jin [2], these observations can be explained by the same coarsening phenomena found in steady state solidification studies, where at long solidification times, coarsening leads to a matrix microstructure where the dendrite features are lost and microsegregation is reduced [11].

Thus, the presence of the SiC particles plays an important role in controlling the development of the

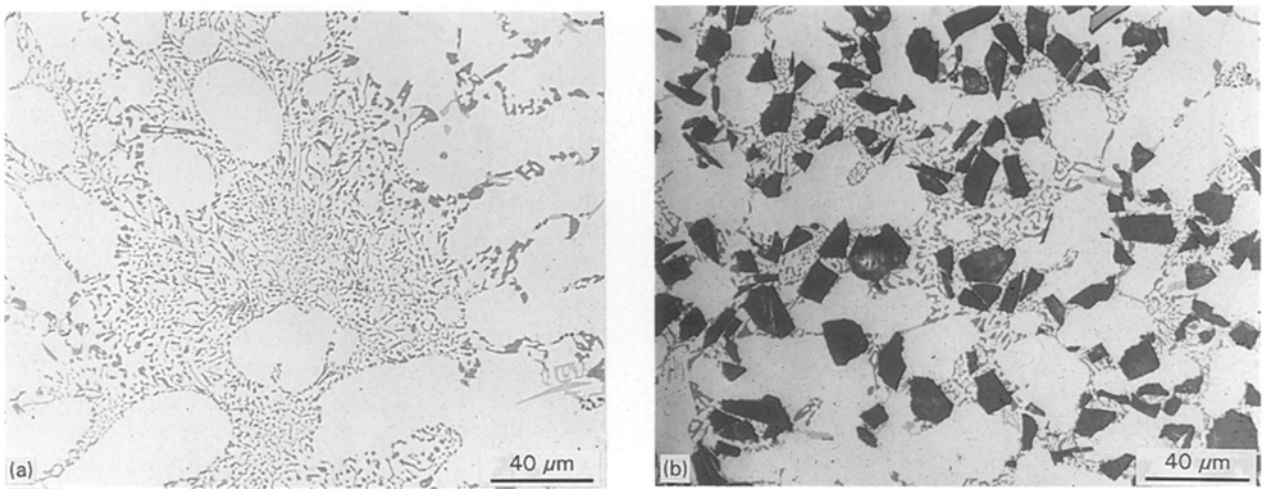

Figure 1 Microstructure of the specimens in the as-cast condition: (a) 359 alloy, (b) composite.

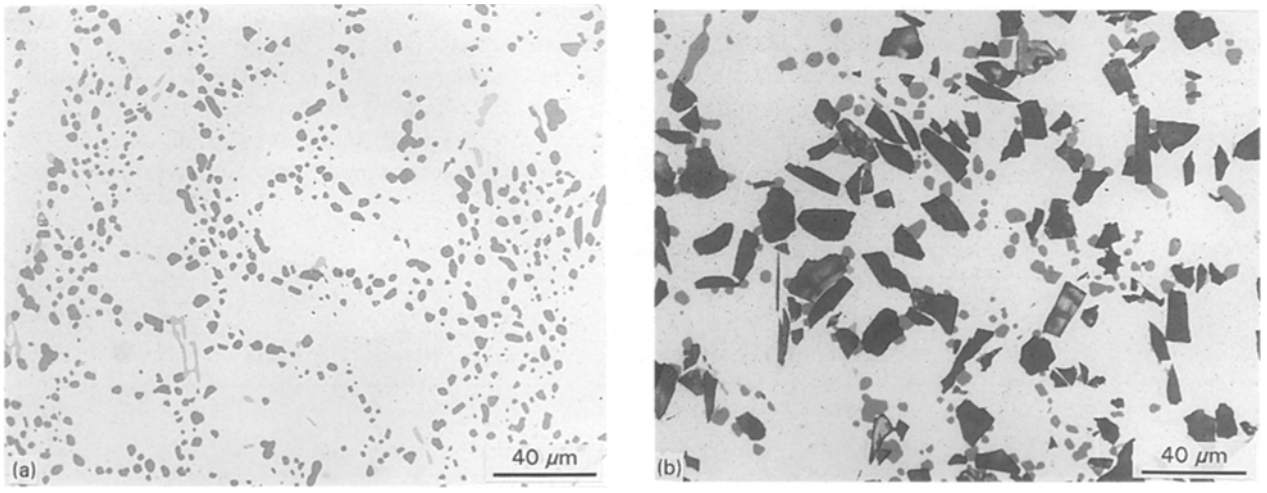

Figure 2 Microstructure of the specimens solutionized for 8 h at 540 °C: (a) 359 alloy, (b) composite.

matrix microstructure. Microstructures of the solution heat treated samples (8 h at 540 °C) of both base alloy and composite, Fig. 2a,b, respectively, confirmed that the solution treatment resulted in complete spheroidization of the Si particles, as reported by the authors elsewhere [12], solution treatment at 540 °C being preferable to that at a higher temperature (550 °C), to avoid the effects of coarsening and grain boundary melting.

3.2. Tensile properties

3.2.1. Modulus of elasticity, E_c

Of a variety of models reported in the composite literature, two models are often used for calculating the average Young's modulus, E_c, of a given composite. The first, known as the "shear–lag" model [13, 14], is based on the mixture rule

$$E_c = E_m f_m + E_p f_p \quad (1)$$

E_m and E_p being, respectively, the moduli of the matrix and particles, and f_m and f_p their volume fractions. Strictly speaking, this model is applicable only to composites reinforced by continuous fibres. The second model, that allows for discontinuous reinforcement, as is the present case, is a modified version of the Tsai–Halpin equation [15]

$$E_c = E_m(1 + 2Sqf_p)/(1 - qf_p) \quad (2)$$

where

$$q = (E_p/E_m - 1)/(E_p/E_m + 2S) \quad (3)$$

and S is the aspect ratio of the particles (~ 1.7 in the present study). The calculated results for SiC particulate reinforced composites are shown in Table II and compared with the measured values. As expected, Equation 2 is seen to be more reasonable than Equation 1.

The work of McDanels [16] on SiC–Al composites containing discontinuous SiC whisker, nodule or particulate reinforcement, shows that the modulus of elasticity is dominantly controlled by the amount of reinforcement, but that for a given reinforcement content, it is actually independent of the type of reinforcement or the matrix alloy. Heat treatment may have a slight effect on the modulus (the lowering of the modulus by 3–4% being within the experimental error). In the present study, ageing was seen to lower the modulus of the as-cast composite by about 5%.

TABLE II Values of the modulus of elasticity, E_c, as a function of SiC_p content

SiC_p (vol %)	E_{meas} (GPa)	$E_{Equation\ 1}$ (GPa)	$E_{Equation\ 2}$ (GPa)	ΔE% (Equation 1)	ΔE% (Equation 2)
0	74.52	74.52	74.52	–	–
10	85.56	111.00	92.80	30	9
20	98.67	147.60	113.70	49	15

$\Delta E = [(E_{cal} - E_{meas})/E_{meas}] \times 100$

3.2.2. Determination of the yield behaviour

According to Taya *et al.* [17], the strengthening of a particulate metal matrix composite during quenching is attributed to two mechanisms

1. punched out dislocations due to the thermal expansion coefficient (CTE) mismatch between the matrix metal and reinforcement, and
2. back stress.

Their analytical study on SiC_p–6061 Al composites (T4 tempered) revealed that the particulate volume fraction and size, the quenching temperature and the temperature differential were the major variables that influenced the increase in composite flow stress compared to that of its matrix.

Referring to the appendix for nomenclature and definition of symbols, Taya *et al.* [17] showed that the yield stress of the composite, σ_c^0, is given by

$$\sigma_c^0 = \sigma_c^0 + \Delta\sigma_{CTE} \quad (4)$$

where

$$\Delta\sigma_{CTE} = \alpha\mu b\bar{\rho}^{(1/2)} \quad (5)$$

and

$$\bar{\rho} = (12\alpha f_p)/ab(1 - f_p) \quad (6)$$

The material properties of the present composite are listed in Table III and show that the calculated value of $\Delta\sigma_{CTE}$ ranges between 50 and 58 MPa.

The variation in yield strength (YS) of the matrix alloy (359) and composite (359–SiC–20p) as a function of ageing temperature and time is shown in Fig. 3, where each reading is an average of the values obtained from at least eight test bars, the standard deviation being about $\pm$ 3% in the case of 359 and $\pm$ 5.5% for the composite. The initial difference between σ_c^0 and σ_m^0, attributed to $\Delta\sigma_{CTE}$ (established during quenching after solution heat treatment), is about 62 MPa. The transmission electron microscopic work of Cottu *et al.* [18] confirms that the presence of the SiC particulates enhances the precipitation kinetics of the Mg_2Si phase, but does not alter it. Thus, the main role of the SiC_p lies in developing a marked $\Delta\sigma_{CTE}$ during quenching following solution heat treatment.

Clegg [19] calculated σ_c^0 using a macroscopic yield criterion, namely the Tresca criterion. His numerical analysis of the stress distribution showed that σ_c^0 is

TABLE III Material properties of the composite

Parameter		Al matrix	SiC particles
Young's modulus	(GPa)	74.52	440
Shear modulus	(GPa)	28.0	–
Burger's vector	(nm)	0.283	–
Average particle radius	(μm)	–	15.21
SiC_p content	(vol %)	–	20
Critical misfit strain		11.6×10^{-3}–2×10^{-4}	–
Interfacial shear strength	(MPa)	140	–
Particle strength	(MPa)	–	2000
Average particle aspect ratio		–	1.7

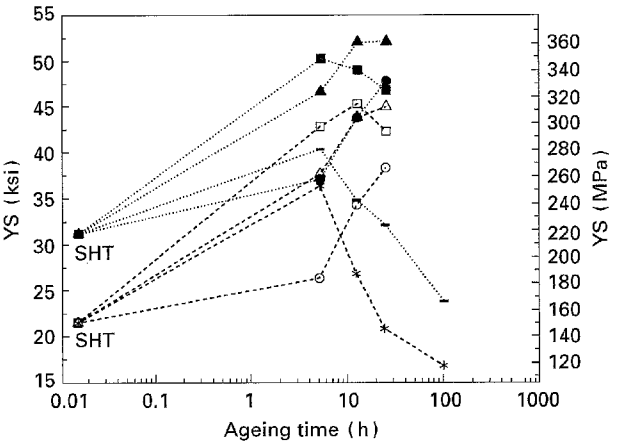

Figure 3 Variation in YS as a function of ageing time at different ageing temperatures. For 359 alloy: (○) 140 °C, (△) 155 °C, (□) 180 °C, (*) 210 °C. For the composite: (●) 140 °C, (▲) 155 °C, (■) 180 °C, (▬) 210 °C.

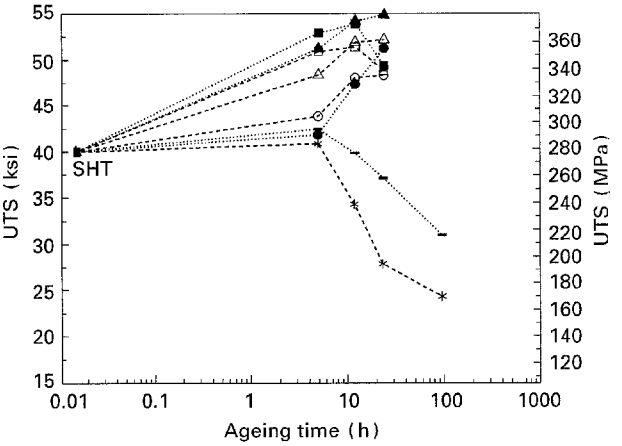

Figure 4 Variation in UTS as a function of ageing time at different ageing temperatures. For 359 alloy: (○) 140 °C, (△) 155 °C, (□) 180 °C, (*) 210 °C. For the composite: (●) 140 °C, (▲) 155 °C, (■) 180 °C, (▬) 210 °C.

related to σ_m^0 by the expression

$$\sigma_c^0 = \sigma_m^0/(1 + b_{33} - b_{11}) \quad (7)$$

where

$$\langle P_{ii}^E \rangle = b_{ii} \times P_{33}^A \quad (8)$$

assuming a homogeneous specimen under an applied uniaxial tension in the x_3 direction, P_{33}^A. His approach shows that σ_m^0 should be much lower than σ_c^0.

Applying the "shear–lag" analysis, Lagacé and Lloyd [20] proposed the following equations

$$S_c = \sigma_p/\tau_i \quad (9)$$

$$\tau_i = \sigma_m^0/2 \quad (10)$$

For $S < S_c$,

$$\sigma_c^0 = \sigma_m^0 (f_p S/4 + f_m) \quad (11)$$

For $S > S_c$,

$$\sigma_c^0 = (f_p \sigma_p/2) + f_m \sigma_m^0 \quad (12)$$

Nardone and Prewo [21] suggested a modified form of Equation 12, based on the edge loading effect

$$\sigma_c^0 = \sigma_m^0 [f_p(S + 4)/4 + f_m] \quad (13)$$

For the present composite, S is about 1.7. Calculating σ_c^0 from Equation 11 for the solution heat treated condition yields values of $\sigma_c^0 \sim 140$ MPa ($\sigma_m^0 \sim 149$ MPa) that are $\sim 70\%$ of those experimentally obtained ($\sigma_c^0 \sim 215$ MPa). In order to arrive at a reasonably acceptable value, one would have to multiply S by a factor of ten. On the other hand, use of Equation 13 would yield values only about 25% lower than those shown in Fig. 3.

3.2.3. Factors influencing ultimate tensile strength, UTS

The effect of heat treatment on the ultimate tensile strength of the present composite and its base alloy are summarized in Fig. 4. The results show that, in general, the ultimate tensile strength of the composite is somewhat higher (21–34 MPa) than that obtained from the similarly heat treated 359 alloy. These results also reaffirm that the presence of a high dislocation density in the matrix of the composite material (caused by the large CTE mismatch strain) accelerates the Mg_2Si precipitation kinetics, as mentioned earlier in connection with Fig. 3. One of the important features of the composite is its resistance to softening on prolonged ageing even at temperatures as high as 210 °C, compared to the base (matrix) alloy (~ 70 MPa higher after 100 h ageing).

From the shape of the stress–strain curves obtained from different wrought alloys reinforced with 15, 20, 30 and 40 vol % SiC_p, McDanels [16] concluded that with increasing reinforcement content, the elastic modulus increased and caused the stress–strain curves to enter plastic flow at a higher flow stress level. The slope of the stress–strain curve also increased as the composite entered plastic flow. This indicates that the strength increase was probably caused by closer packing of the reinforcement, which would result in an increased interaction of the dislocations with the SiC_p, that would, in turn, result in increased work hardening.

Typical stress–strain curves obtained from the present foundry alloy 359 and its composite (359–SiC–20p) are shown in Fig. 5a, b, respectively. Both alloys were artificially aged for 5 h at 155 °C (this treatment is the one most commonly employed in the aluminum industry). The variation in the work hardening rate, $\dot{\theta}$, as a function of plastic strain is given in Fig. 6 ($\dot{\theta} = d\sigma/d\varepsilon$). Although the 359 alloy exhibited a higher $\dot{\theta}$ initially (starting with a much lower YS as compared to the composite, but reaching similar UTS levels), the total linear work hardening rate, $\ddot{\theta}$, as given by

$$\ddot{\theta} = (\sigma_{UTS} - \sigma_{YS})/(\varepsilon_{max} - 0.2) \quad (14)$$

was about 18 MPa for the 359 alloy and 39 MPa for the composite, Fig. 6.

The numerical treatment carried out by Clegg [19] shows that once plastic flow of a composite material has commenced, there will be an additional contribution to the back stress due to the plastic misfit, given by

$$\langle P_{ii}^p \rangle_m = q_{ii} \times \varepsilon \quad (15)$$

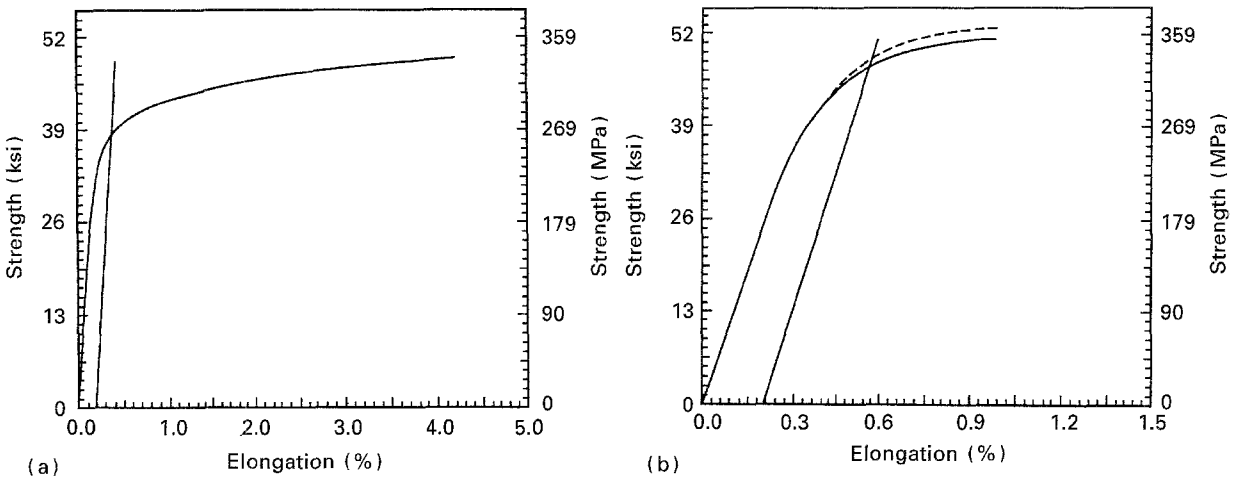

Figure 5 Typical stress–strain curves of specimens aged for 5 h at 155 °C: (a) 359 alloy, (b) composite. In Fig. 5b, the broken line represents theoretical data.

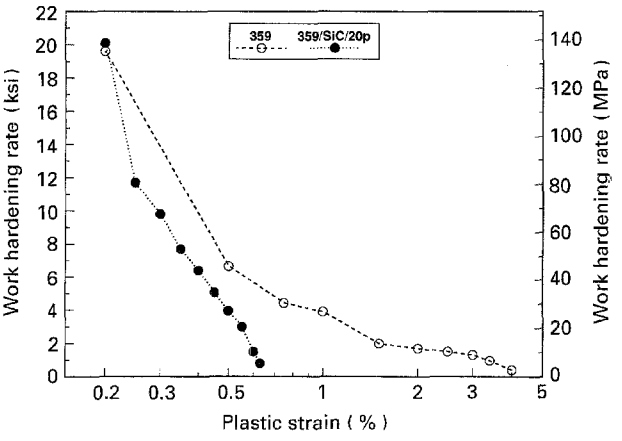

Figure 6 Variation in the work hardening rate as a function of plastic strain: (○) 359 alloy, (●) composite.

The proof stress, P_c^{ps}, is determined by

$$P_c^{ps} = \sigma_c^0 + \varepsilon^{ps} \times \ddot{\theta}/(1 - \ddot{\theta}/E_c) \quad (16)$$

and the increase in flow stress of the matrix for a composite containing equiaxed particles (reinforcement), is given by

$$\Delta P_m^F = k \times E_c \left(\frac{f_p}{1 - f_p} \times \frac{b}{a} \times \varepsilon \right)^{1/2} \quad (17)$$

where $k = 0.62$.

Fig. 5b shows the excellent agreement between the predicted stress–strain curves using Clegg's theoretical approach and the present experimental data.

3.2.4. Strength–elongation relationships

Various events occurring during the ageing treatment can be analysed by plotting the UTS as a function of elongation, Fig. 7a–d, for the base alloy and its composite. As precipitation of Mg_2Si takes place (e.g. during the 5 h ageing period), the 359 alloy, Fig. 7a, and composite, Fig. 7b, undergo hardening, with a noticeable decrease in their ductilities. Both materials attain peak strength at 180 °C, which corresponds to their minimum ductilities.

After a sufficiently long period of ageing (e.g. 24 h), Fig. 7c, d, it is observed that maximum hardening occurs at 155 °C instead of 180 °C. It is interesting to note that at the ageing temperature 210 °C, though 359 alloy exhibits a ductility close to that obtained in the solution heat treated condition (SHT), the associated strength level is significantly lower than the SHT one. As mentioned previously, the addition of 20 vol % SiC_p to the 359 alloy improves the alloy resistance to softening. The increase in the composite ductility at this temperature after 24 h, however, may indicate the effectiveness of Orowan looping and its progress with increase in ageing time, as was also the case observed after 100 h ageing (not shown here; see [22]).

Purvis and Pehlke [23] suggested that in order to correlate the quality index value with the mechanical properties, three pertinent empirical relationships must be established

$$\text{PYS} = a_1(\text{UTS}) - a_2 \log \text{El} - a_3 \quad (18)$$

$$\text{UTS} = b_1 (\text{RE}) + b_2 \quad (19)$$

$$Q = \text{UTS} + k \log \text{El} \quad (20)$$

where PYS is defined as the probable (or predicted) yield strength, RE is the Rockwell hardness, and a_1, a_2, a_3, b_1, b_2 and k are empirical constants.

Using the data obtained in the present work, these constants are obtained as follows. For the 359 alloy, two sets of a_i constants are developed depending upon the ageing temperature. In the temperature range 140–180 °C, Equation 18 can be written as

$$\text{PYS(MPa)} = 1.5 \times \text{UTS(MPa)} + 0.2 \times \log \text{El} - 270 \quad (21)$$

whereas at an ageing temperature 210 °C, the equation must be modified to take into account the rapid softening effect caused by overageing, as

$$\text{PYS(MPa)} = 1.8 \times \text{UTS(MPa)} + 0.4 \times \log \text{El} - 203 \quad (22)$$

In the case of the composite, two expressions for Equation 18 were developed, depending on the attained strain. For $\varepsilon < 1\%$

$$\text{PYS(MPa)} = 0.6 \times \text{UTS(MPa)} - 37 \times \log \text{El} + 117.3 \quad (23)$$

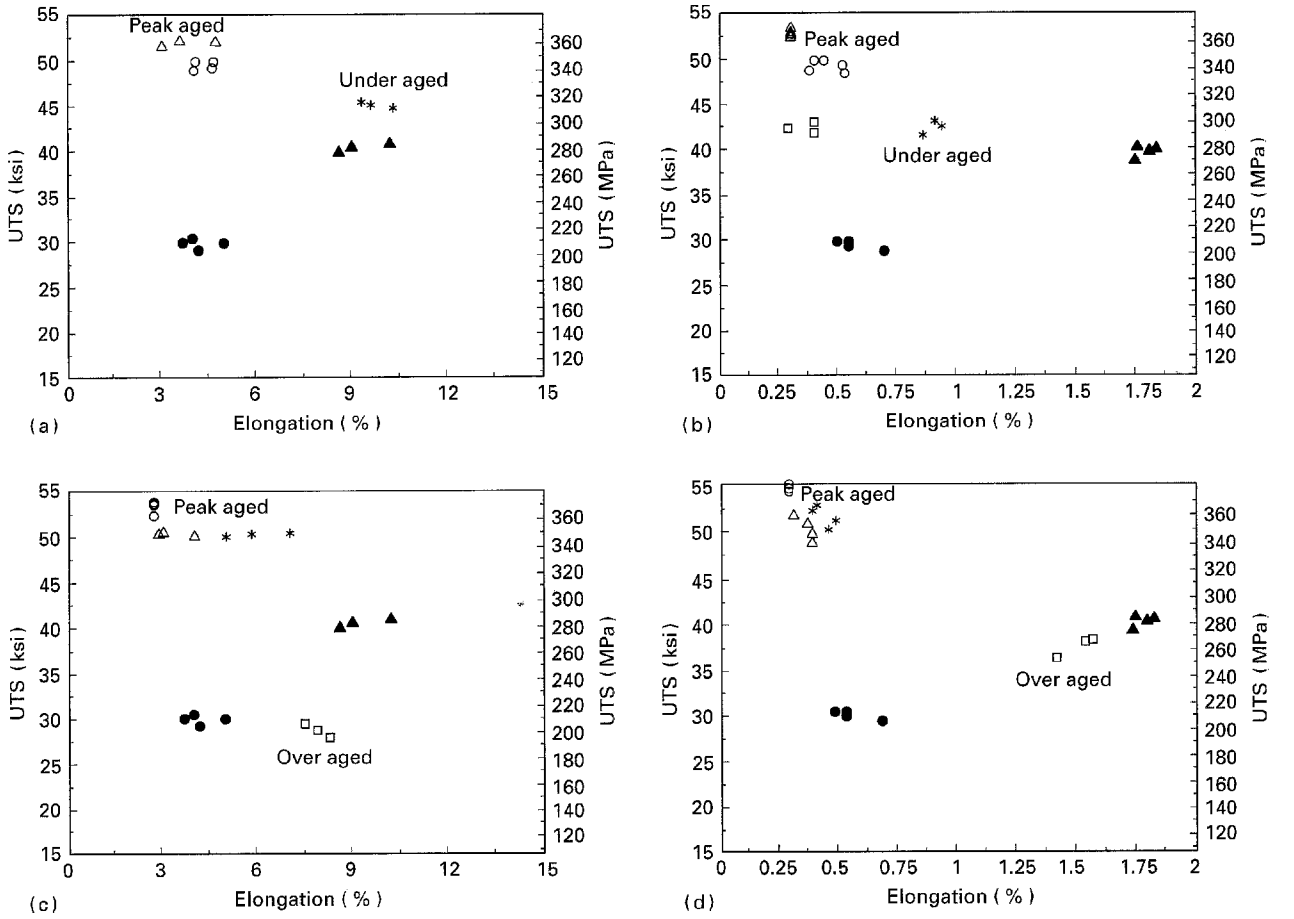

Figure 7 UTS–elongation relationships for: (a) 359 alloy, aged for 5 h at different temperatures; (b) composite, aged for 5 h at different temperatures; (c) 359 alloy aged for 24 h at different temperatures; (d) composite aged for 24 h at different temperatures. (●) As-cast, (▲) SHT, (*) 140 °C, (○) 155 °C, (△) 180 °C, (□) 210 °C.

For $\varepsilon > 1\%$

$$\text{PYS(MPa)} = 0.4 \times \text{UTS(MPa)} - 40 \times \log \text{El} + 124 \quad (24)$$

The statistical correlation coefficient, R, for these two equations was fairly low due to data scatter caused by the variations in the solidification conditions and melt cleanliness. Purvis and Pehlke [23] have also reported similar observations of low R values for 319 alloy.

The quality index, Q, developed by Drouzy *et al.* [24] has often been used to interpret tensile data. As shown in Equation 20, the quality index has been defined in MPa units as

$$Q\,(\text{MPa}) = \text{UTS(MPa)} + 150 \log \text{El} \quad (25)$$

The work of Shivkumar *et al.* on 356 alloy [25] shows that the Q values are not significantly affected by the ageing conditions. However, Q is a function of $t^{1/3}$ (t being the solution time at 540 °C), and varies almost linearly with the eutectic Si particle size and count.

The UTS values were correlated with elongation (or log elongation) to obtain Q. Plots were obtained of the form

$$\text{UTS} = a + b \times \text{El} \quad (26)$$

or

$$\text{UTS} = a + b \times \log \text{El} \quad (27)$$

a being the intercept with the y-axis, and b the slope, to determine the best fit with respect to the ageing temperature. Fig. 8a represents the graph of the points for UTS versus El for the 359 alloy. The obtained values for a and b are listed in Table IV. It can be seen from Fig. 8a that ageing at 140 or 155 °C (which represent under and peak ageing, respectively) produces similar relationships which, however, are significantly different from those obtained at 210 °C (over-aged condition). Thus, in Fig. 8b, all points for the temperature range 140–180 °C are regrouped together for a better representation.

The plot of UTS versus log El for 359 alloy is shown in Fig. 8c. Three distinct lines are obtained for the under, peak and overaged conditions. The slopes for ageing temperatures 140 and 155 °C are very close to that reported for 356 alloy (containing 7 wt % Si and 0.35 wt % Mg). Regrouping all the points for the ageing temperature range 140–180 °C yields a good linear relationship, Fig. 8d (see also Table V). However, the slope obtained is lower than that reported in Equation 25.

The UTS versus El relationship for the composite is shown in Fig. 9a. As can be seen, the points are more or less randomly distributed, with poor correlation coefficient, R, values (see Table VI). Regrouping all points for the ageing temperature range 140–210 °C, a much better correlation is obtained ($R \sim 0.8$), Fig. 9b. Fig. 9c shows that much better relationships are obtained on plotting UTS versus log El (see Table VII). The points could be arranged in two lines that were almost parallel, with slopes close to that given in

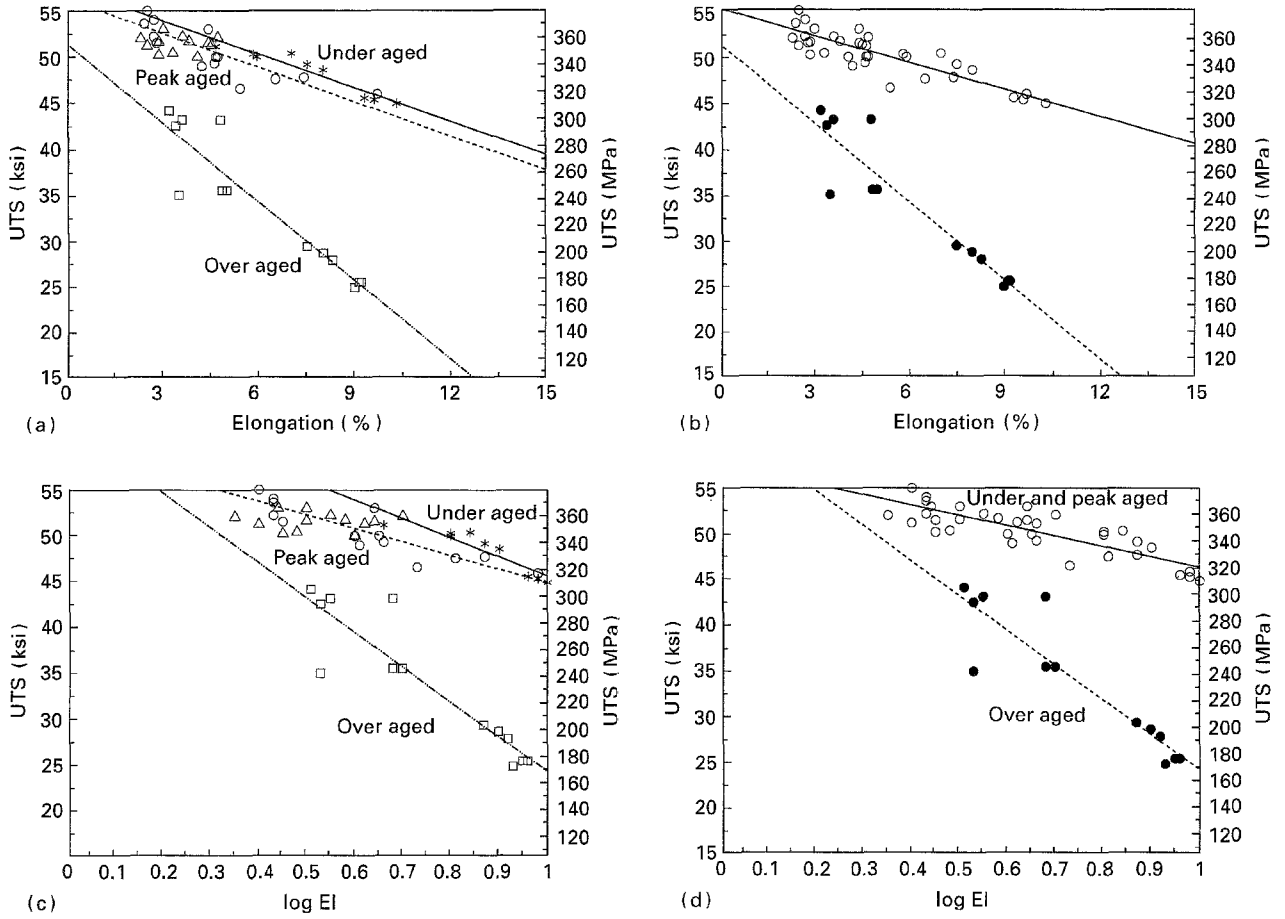

Figure 8 UTS–elongation relationships for (a) 359 alloy at different ageing temperatures (*) 140 °C, (○) 155 °C, (△) 180 °C, (□) 210 °C; (b) UTS-log elongation relationships for 359 alloy, (—○—) ageing temperatures 140–180 °C and (--●--) 210 °C; (c) UTS–log elongation relationships for 359 alloy at different ageing temperatures (*) 140 °C, (○) 155 °C, (△) 180 °C, (□) 210 °C; and (d) UTS–log elongation relationships for 359 alloy, (—○—) ageing temperatures 140–180 °C and (--●--) 210 °C.

TABLE IV UTS–El relationships for 359 alloy

Ageing temperature (°C)	*a* (MPa)	*b* (MPa)	R^a
140	396.54	− 8.27	0.906
155	388.00	− 8.46	0.746
180	358.80	− 0.90	0.011
$(140–180)_{av}$	380.30	− 6.61	0.740
210	354.60	− 19.62	0.870

[a] *R*, statistical correlation coefficient.

TABLE V UTS–log El relationships for 359 alloy

Ageing temperature (°C)	*a* (MPa)	*b* (MPa)	R^a
140	456.78	− 141.450	0.830
155	411.24	− 100.740	0.810
180	357.60	− 3.726	(scatter)
$(140–180)_{av}$	397.09	− 76.310	0.690
210	428.90	− 260.130	0.838

[a] *R*, statistical correlation coefficient.

Equation 25 for 356 alloy. The best fit was obtained when all points in the 140–210 °C range were represented by a single line, as shown in Fig. 9d, instead of two lines, as in the case of 359 alloy, Fig. 8d. This highlights the importance of the 359–SiC–20p composite, in that its tensile properties can be predicted/determined over the entire ageing temperature range.

3.3. Fractography

Gangulee and Gurland [26] have proposed that fracture in Al–Si alloys occurs in three stages

1. crack initiation at the Si particles,
2. propagation of the cracks in the interdendritic regions, and
3. rupture of the matrix.

Fig. 10a, b exhibits the transverse sections through the fracture planes of 359 samples in the as-cast and aged (5 h at 155 °C) conditions, respectively. It is evident that the rupture mechanism is not affected by the material strength. Crack propagation occurs through the interdendritic regions, when the dendrites are pulled to rupture, leaving sharp pointed ends that appear aligned nearly parallel to the loading axis (arrowed).

The fracture surface of the composite in the as-cast condition is shown in Fig. 11a. The crack occurs in the matrix by the void nucleation and growth mechanism. In this case, it is difficult to perceive the SiC particles. Examination of the polished section beneath the fracture surface, Fig. 11b, reveals features similar to those observed in Fig. 10a for the base alloy. The fracture shows how the crack opens in the aluminum matrix

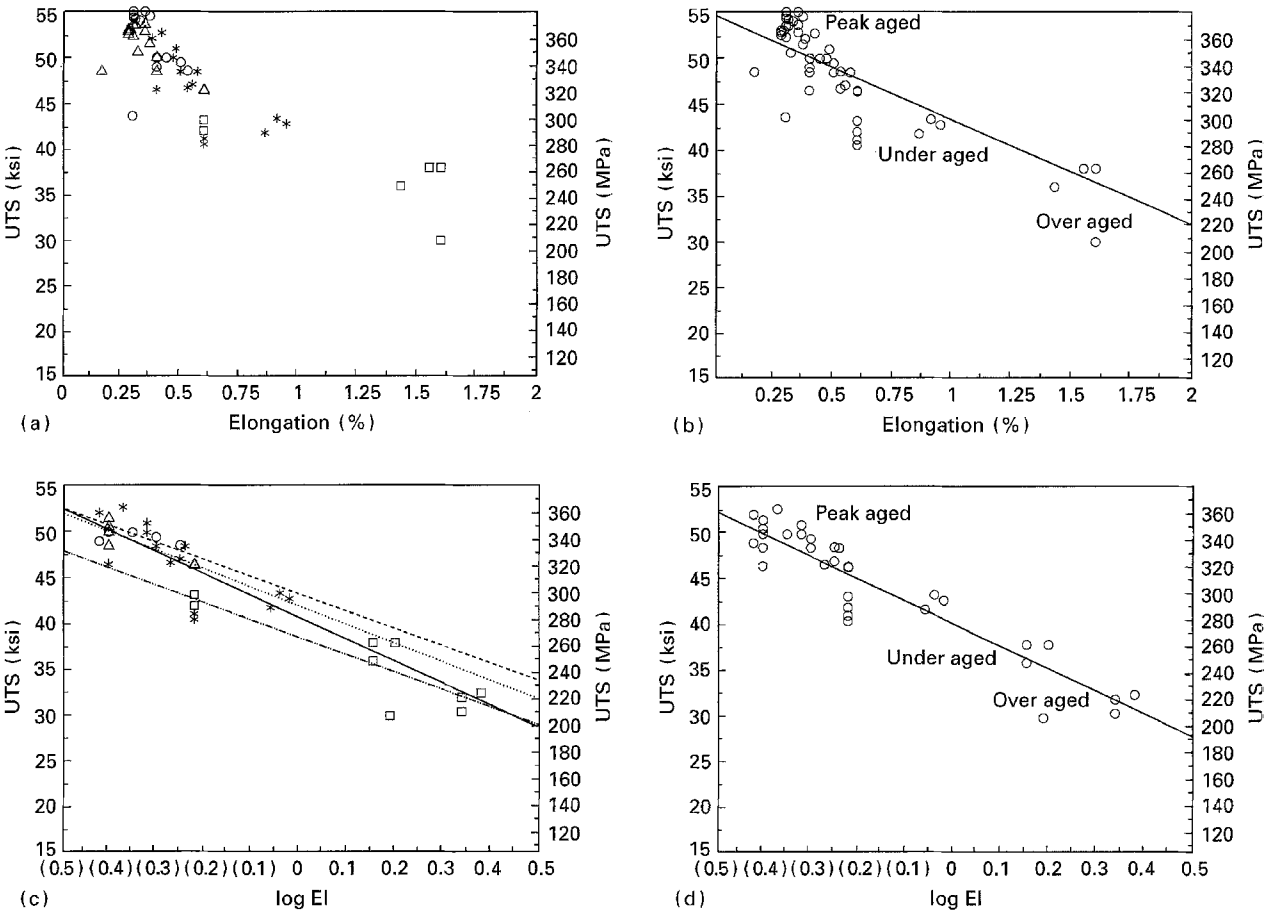

Figure 9 UTS–elongation relationships for (a) the composite at different ageing temperatures, (b) for the composite. Points corresponding to ageing temperatures 140–210 °C are represented by a single line. (c) UTS–log elongation relationships for the composite at different ageing temperatures. (d) UTS–log elongation relationships for the composite. Points corresponding to ageing temperatures 140–210 °C are represented by a single line. (*) 140 °C, (○) 155 °C, (△) 180 °C, (□) 210 °C.

TABLE VI UTS–El relationships for the composite

Ageing temperature (°C)	a (MPa)	b (MPa)	R^a
140	380.880	− 107.90	0.502
155	408.750	− 138.00	0.201
180	388.500	− 100.88	0.436
210	316.158	− 43.74	0.734
$(140–210)_{av}$	377.800	− 78.84	0.800

[a] R, statistical correlation coefficient.

TABLE VII UTS–log El relationships for the composite

Ageing temperature (°C)	a (MPa)	b (MPa)	R^a
140	281.16	− 164.35	0.550
155	298.77	− 129.23	0.283
180	289.80	− 139.93	0.733
210	266.18	− 130.65	0.760
$(140–210)_{av}$	277.80	− 168.84	0.870

[a] R, statistical correlation coefficient.

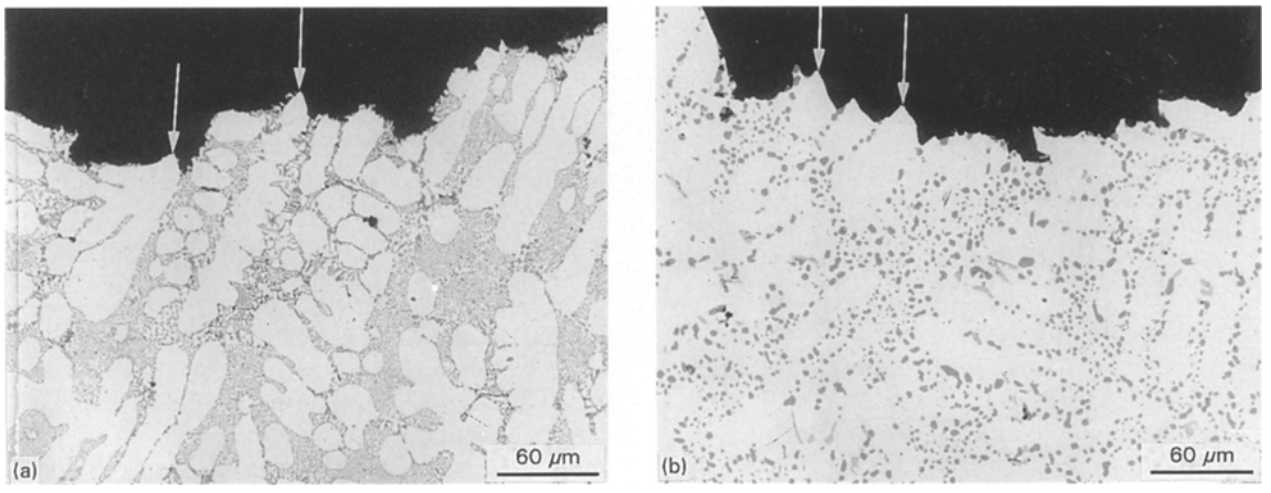

Figure 10 Microstructure of 359 alloy beneath the fracture surface: (a) as-cast, (b) aged 5 h at 155 °C.

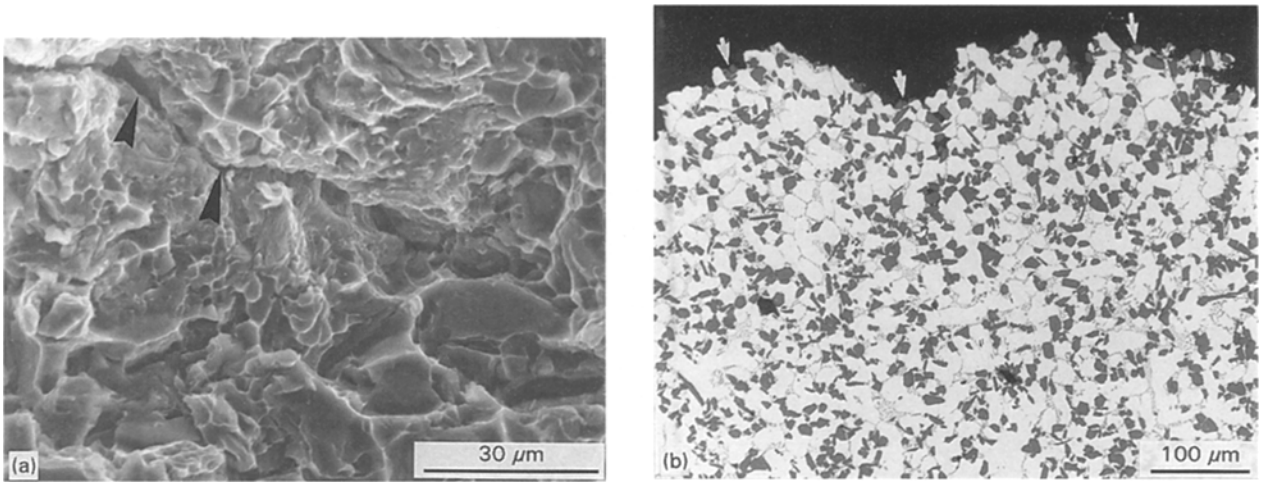

Figure 11 Fracture surface (a) and microstructure beneath the fracture surface (b) for the composite in the as-cast condition.

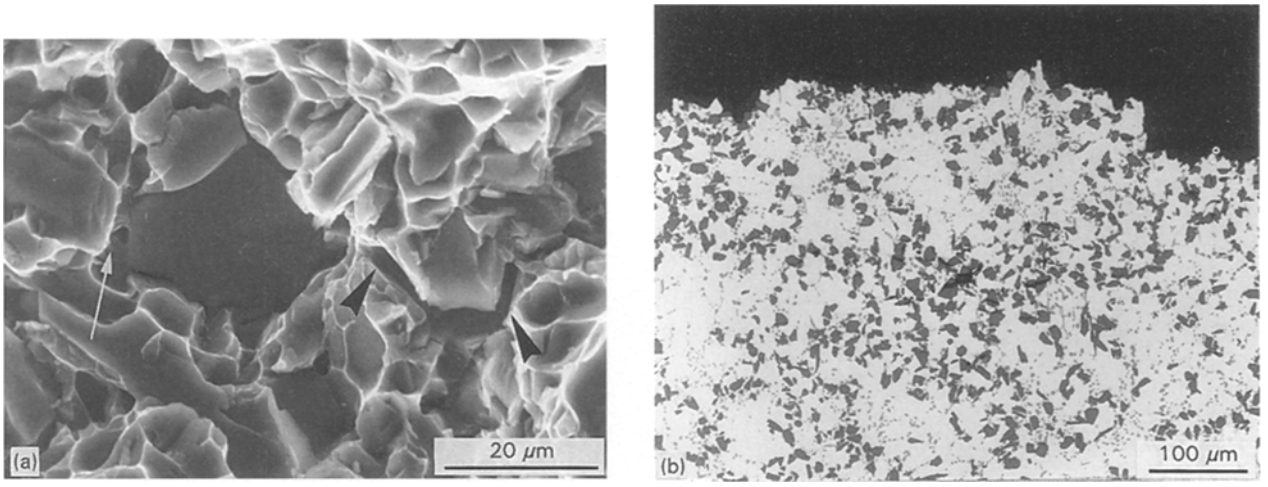

Figure 12 Fracture surface (a) and microstructure beneath the fracture surface (b) for the composite in the solution heat treated condition.

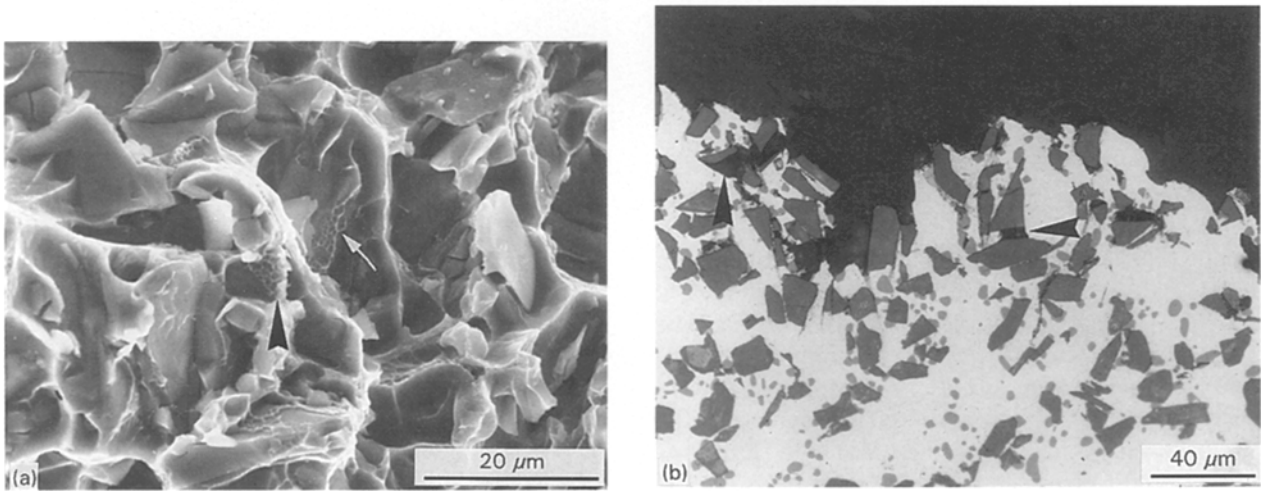

Figure 13 Fracture surface (a) and microstructure beneath the fracture surface (b) for the composite aged 5 h at 140 °C.

and extends either by traversing through the particle–matrix interface or by shearing the SiC particles depending on the particle–matrix adhesion force.

The typical fracture surface obtained from solution heat treated samples of the composite is shown in Fig. 12a, where a few SiC particles are present. Dimples in the matrix are coarse, whereas those located in the spaces between the SiC related dimples are very fine (white arrows). Voids are also observed at the particle–matrix interface (black arrows). The polished longitudinal section of specimens obtained from the tensile tested bars, Fig. 12b, revealed the presence

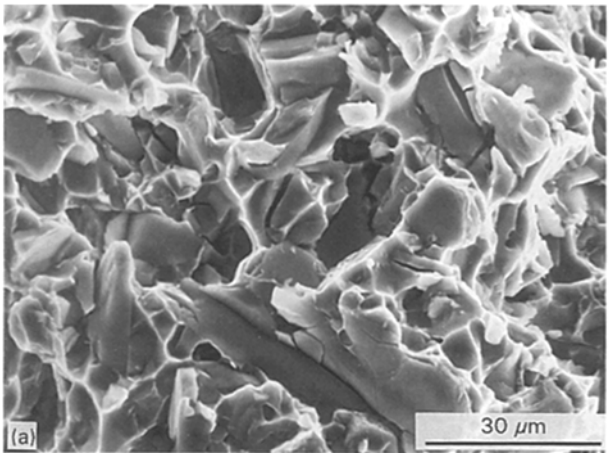

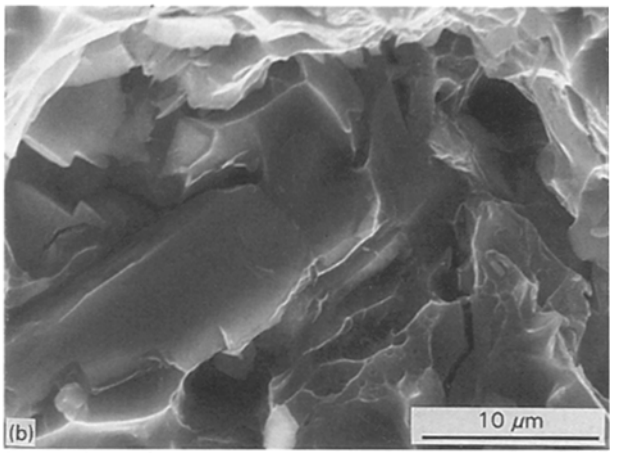

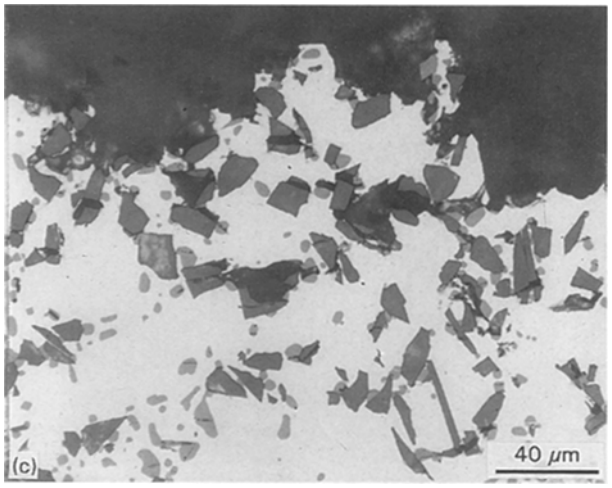

Figure 14 Fracture surface (a, b) and microstructure beneath the fracture surface (c) for the composite aged 5 h at 155 °C.

of fractured SiC particles, normal to the tensile axis.

Fracture surfaces of composite samples in the underaged condition (5 h at 140 °C) reveal two operating fracture mechanisms: microvoid formation and SiC particle cracking, Fig. 13a. The SiC–matrix interface is made up of a network of very fine dimples, as shown by the arrows. The longitudinal polished section, Fig. 13b, reveals the depth of the damage caused by plastic deformation beneath the fracture surface. Voids are mostly seen to be nucleated at the bottom of the SiC particles.

The extent of SiC particle cracking appears to be greater after 5 h ageing time at 155 °C than after 5 h at 140 °C. This is evident from a comparison of Figs 14a and 13a, indicating a strong SiC–Al bonding. The number of broken particles was maximum in the vicinity of the fracture surface. A high magnification micrograph, Fig. 14b, reveals the severe damage of the SiC particles, which seems to be the main characteristic feature of the fracture mode. This observation is further confirmed by examining the polished section beneath the fracture surface, Fig. 14c. Note, also, the increase in the depth of the damaged zone, cf. Fig. 13b.

In the peak aged condition (5 h at 180 °C), Fig. 15a, the principal features remain more or less the same as those reported above. Examination of the longitudinal polished section beneath the fracture surface, Fig. 15b, reveals that this condition results in the most severe damage to the SiC particles either by cracking or

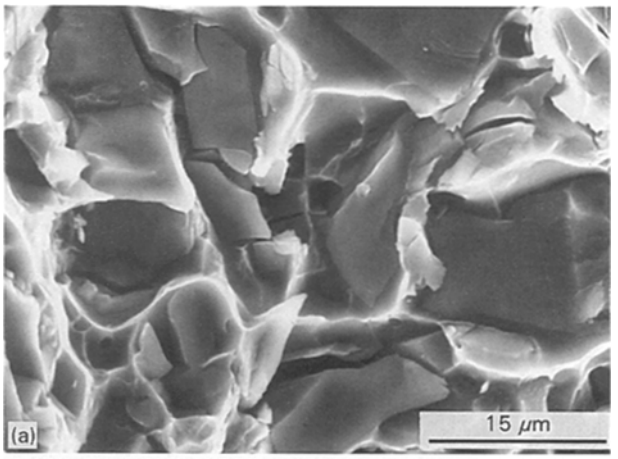

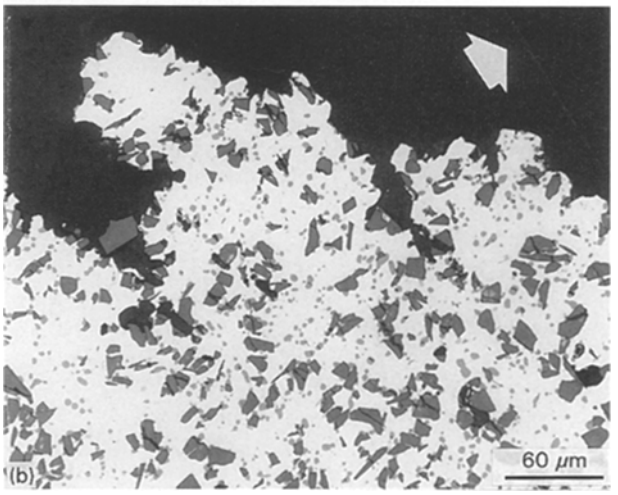

Figure 15 Fracture surface (a) and microstructure beneath the fracture surface (b) for the composite aged 5 h at 180 °C. The arrow in Fig. 15b indicates the direction of tensile loading.

voiding, and this effect extends over a large distance underneath the fracture surface.

In the overaged condition, 5 h at 210 °C, Fig. 16a, the fracture surface resembles that obtained after solution treatment, Fig. 12a. It should be noted that the strength and ductility values in the two conditions are found to be almost identical (see Fig. 7). The polished

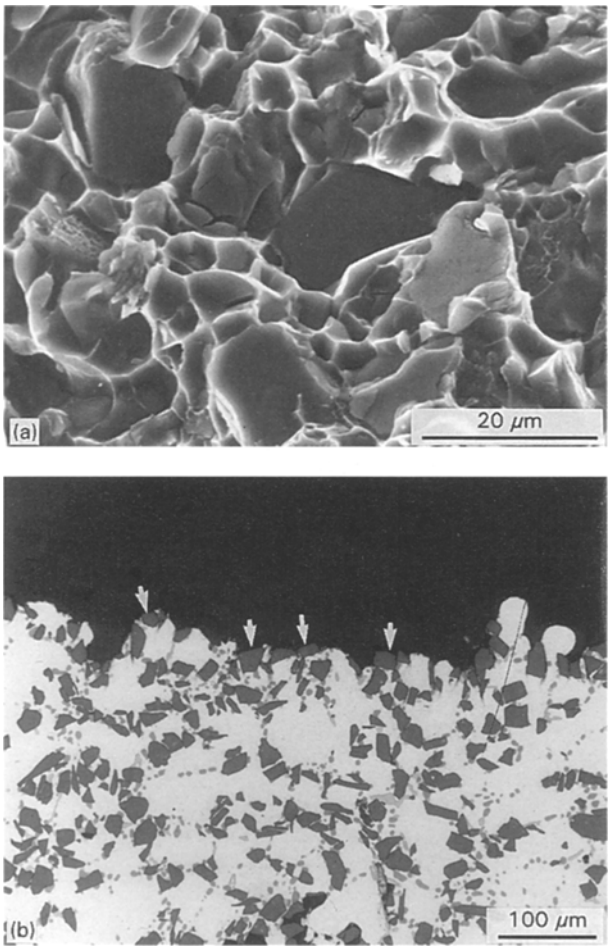

Figure 16 Fracture surface (a) and microstructure beneath the fracture surface (b) for the composite aged 5 h at 210 °C.

section transverse to the fracture surface, Fig. 16b, reveals that the crack mainly occurs at the SiC–Al matrix interface, with no noticeable SiC particle cracking as that observed in Fig. 16a.

The relationship between heat treatment and the number of broken SiC particles observed in the corresponding heat treated test bars pulled to fracture is summarized in Table VIII. It is found that there is an increase in the number of broken particles with increasing tensile strength. The SiC particles were measured over an area 1 mm thick (practically representing the extent of the damage zone in which broken particles were observed) and 10 mm wide (taking into account the effect of shear lip near the edges) beneath the rupture surface. Similar observations have been reported by Singh and Lewandowski [6] on 7XXX–SiC–15p composites, for a given particulate size ($\sim$ 13 μm). It should be noted that in their work, the number of broken SiC particles was measured over an area of $\sim 12.7 \times 2.3$ mm (specimen gauge length) × (specimen width) which gives nearly the same surface area as that measured in the present case. The difference in the number of broken SiC particles observed in their case and the present study is explained by the difference in the amount of global plastic strain obtained in the two cases (i.e. 8 versus 0.6%, respectively), resulting from the nature of the respective matrix alloys used (wrought versus cast).

TABLE VIII Relationship between heat treatment and number of broken SiC particles in composite test bars pulled to fracture

Condition	UTS (MPa)	El (%)	No. of broken SiC_p [a]	% of broken SiC_p [a]
As-cast	210.5	0.80	880	1.12
SHT	279.0	2.10	3240	4.14
5 h/140 °C (underaged)	299.5	0.82	10000	12.60
5 h/155 °C (underaged)	344.0	0.58	13600	17.40
5 h/180 °C (peakaged)	366.0	0.45	22440	28.70
5 h/210 °C (overaged)	298.0	1.20	1600	2.00

[a] Total number of SiC particles: $\sim$ 78300 over an examined area of $\sim$ 20 mm^2.

4. Conclusions

From an analysis of the microstructural, tensile test and fractographic observations made during a study of as-cast and heat treated 359–SiC–20p composite and its base alloy (359), the following are found

1. Addition of SiC_p reinforcement to 359 alloy results in a more uniform and refined interdendritic microstructure (cf. the large, irregular interdendritic regions observed in the base alloy).

2. A comparison of the experimentally obtained modulus of elasticity, E_c, value with those calculated from the "shear–lag" or Tsai–Halpin models shows that the latter is more representative of the experimental data for the present composite. Ageing is found to lower E_c by about 5%. The stress–strain curves for artificially aged composite (5 h at 155 °C) show excellent agreement with the predicted stress–strain curves proposed by Clegg [19].

3. The SiC particles are instrumental in developing a marked difference in the yield stress, σ^0, of the composite and base alloy, $\sigma_c^0 - \sigma_m^0 \simeq 62$ MPa, during quenching following solution heat treatment. No significant contribution to σ_c^0 is obtained on subsequent artificial ageing, indicating that while the presence of the SiC particles accelerates the precipitation kinetics of the Mg_2Si phase, it does not alter it.

4. Strength–elongation relationships for the composite show that SiC_p addition to the base alloy improves the alloy resistance to softening. This effect is observed even at an ageing temperature of 210 °C for long ageing times. The tensile properties of the composite can be predicted over the entire ageing temperature range studied (140–210 °C) on a UTS versus log El plot.

5. In the as-cast condition, the composite fracture occurs in the matrix by void nucleation and growth process; in the underaged (5 h at 140 °C) and peak-aged (5 h at 180 °C) conditions, microvoid formation and SiC particle cracking are the operating mechanisms, the peak-aged condition resulting in the maximum damage to the SiC particles and which extends over a large distance underneath the fracture surface; in the overaged (5 h at 210 °C) condition, the fracture

surface resembles that obtained after solution treatment, namely a mixture of coarse and fine dimples together with voids observed at the particle–matrix interface.

Acknowledgements

The authors would like to thank Duralcan Canada, Usine Dubuc, Chicoutimi, Québec for supplying the composite material. They also wish to thank Dr H. Liu for his help with the scanning electron microscopy work. Financial support received from the Natural Sciences and Engineering Research Council of Canada is gratefully acknowledged.

References

1. G. A. CHADWICK, *Cast Metals*, **4** (1991) 165.
2. A. MORTENSEN and I. JIN, *Int. Mater. Rev.* **37** (1992) 101.
3. P. K. LIAW and M. GUNGOR (Eds), "Fundamental Relationships Between Microstructure and Mechanical Behavior of Metal Matrix Composites", Transactions of the Minerals, Metals and Materials Society (American Institute of Mining, Metallurgy and Petroleum Engineering, Warrendale, PA, 1990).
4. G. A. ROZAK, *et al.*, *J. Compos. Mater.* **26** (1992) 2076.
5. W. H. HUNT, Jr. T. M. OSMAN and J. J. LEWANDOWSKI, *JOM* **45** (1993) 30.
6. P. M. SINGH and J. J. LEWANDOWSKI, *Metall. Trans. A* **24A** (1993) 2531.
7. C. DUPUIS, Z. WANG, J.-P. MARTIN and C. ALLARD, "Light, Metals 1992", edited by E. R. Cutshall (The Minerals, Metals and Materials Society, Warrendale, PA, 1991), pp. 1055–1068.
8. ASTM Standards, "Standard Specification for Aluminum Alloy Permanent Mold Castings", ASTM 02.02 (American Society for Testing and Materials, Philadelphia, PA, 1990) pp. 104–113.
9. A. M. SAMUEL, H. LIU and F. H. SAMUEL, *Compos. Sci. Technol.* **49** (1993) 1.
10. M. A. BAYOUMI and M. SUÉRY, in "Cast Reinforced Metal Composites", edited by S. G. Fishman and A. K. Dhingra, (American Society for Metals International, Metals Park, OH, 1988) pp. 167–172.
11. A. MORTENSEN, J. A. CORNIE and M. C. FLEMINGS, *Metall. Trans. A.* **19A** (1988) 709.
12. A. M. SAMUEL and F. H. SAMUEL, *J. Mater. Sci.* **29** (1994) 3591.
13. H. L. COX, *Br. J. Appl. Phys.* **3** (1952) 72.
14. M. R. PIGGOT, "Load Bearing Fibre Composites" (Pergamon Press, Oxford, 1980).
15. J. C. HALPIN, "Primer on Composite Materials: Analysis" (Technomic Publ., PA).
16. D. L. McDANELS, *Metall. Trans. A.* **16A** (1985) 1105.
17. M. TAYA, K. E. LULAY and D. J. LLOYD, *Acta Metall. Mater.* **39** (1991) 73.
18. J.-P. COTTU, J.-J. COUDERC, B. VIGUIER and L. BERNARD, *J. Mater. Sci.* **27** (1992) 3068.
19. W. J. CLEGG, *Acta Metall.* **36** (1988) 2141.
20. H. LAGACÉ and D. J. LLOYD, *Can. Metall. Quart.* **28** (1989) 145.
21. V. C. NARDONE and K. M. PREWO, *Scripta Metall.* **20** (1986) 43.
22. F. H. SAMUEL and A. M. SAMUEL, *Metall. Mater. Trans. A* **25A** (1994) 2247.
23. A. L. PURVIS and R. D. PEHLKE, *AFS Trans.* **96** (1988) 539.
24. M. DROUZY, S. JACOB and M. RICHARD, *Fonderie* **31** (1976) 139.
25. S. SHIVKUMAR, S. RICCI, Jr. B. STEENHOFF, D. APELIAN and G. SIGWORTH, *AFS Trans.* **97** (1989) 791.
26. A. GANGULEE and J. GURLAND, *Trans. Metall. Soc. AIME* **239** (1967) 239.

Received 28 June
and accepted 21 September 1994